Laser annealing of Au/HfO$_2$ bi-layers to fabricate Au nanoparticles without altering the phase of HfO$_2$ for applications in SERS and memory devices

K. Vinod Kumar[1], J. Pundareekam Goud[1], Kanaka Ravi Kumar[1], K. C. James Raju[1,2,*], and S. V. S. Nageswara Rao[1,2,*] (ORCID)

[1] *School of Physics, University of Hyderabad, Hyderabad 500046, India*

[2] *Centre for Advanced Studies in Electronics Science and Technology (CASEST), School of Physics, University of Hyderabad, Hyderabad 500046, India*

ABSTRACT

We report an athermal laser annealing technique to fabricate a high-density array of gold nanoparticles on the surface of hafnium oxide thin films without altering the phase of HfO$_2$. Au ($\sim$ 5 nm) films deposited on amorphous HfO$_2$ ($\sim$ 10 nm) are subjected to laser annealing by using an Excimer laser (248 nm) to produce Au nanoparticles. It is important to note that the usual thermal methods would change the phase of the HfO$_2$. It is observed that the size of the spherical Au nanoparticles decreases and their surface density increases as the number of laser pulses increases. These Au nanoparticles has induced a significant enhancement in the Raman signature of the standard R6G dye. Further, Metal–Oxide–Semiconductor capacitors were fabricated by depositing another layer of HfO$_2$ followed by metal contacts on the surface of these nanoparticles. The leakage current conduction through the gate oxide with and without embedded nanoparticles has been studied using the Poole–Frenkel and Fowler–Nordheim tunneling mechanisms by examining the leakage current–voltage characteristics. PF tunneling is found to be prominent in these MOS structures with Au nanoparticles, which is attributed to the possible charge trapping by the embedded Au nanoparticles. The capacitance–voltage (C–V) characteristics show a significant broadening in the hysteresis loop indicating the improvement in the storage capacity of these MOS capacitors.

Address correspondence to E-mail: kcjrsp@uohyd.ac.in; svnsp@uohyd.ac.in

Springer

1 Introduction

In modern portable electronics, non-volatile memory (NVM) devices have gained attention due to the enormous demand for high-speed and large-storage-capacity devices [1]. Most importantly, floating gate memory devices have received significant attention in recent years due to their low operating voltages and long retention times [2, 3]. To improve the performance, down-scaling of size of the memory devices has been the preferred route [4]. This resulted in a severe challenge as the thinner oxide layer of floating gate flash memories will degenerate retention characteristics because of high leakage currents through the gate oxide due to tunneling [5]. In order to overcome these problems, high-k dielectric materials have been introduced in the industry to replace SiO_2 [6, 7]. Among the many high-k dielectric materials, hafnium oxide (HfO_2) with moderate dielectric constant (k $\sim$ 25) and band gap of 5.3 $\sim$ 5.7 eV can be used in different optoelectronic applications [8]. Moreover, it can form a good interface and has better thermal stability with silicon [9, 10]. Further, HfO_2 also finds applications in spintronic devices as thin insulating barriers for magnetic (spin-dependent) tunnel junctions due its high heat of formation [11]. HfO_2 allows the formation of pinhole-free tunnel barriers with significant transmission of spin polarization of the tunneling electrons [11, 12]. HfO_2 with spin–orbit interaction may have a significant effect on the Anomalous Hall Effect [13, 14]. The material has also got the potential for applications in the devices based on the topological insulators [15, 16].

In the current generation of Metal–Oxide–Semiconductor Field Effect Transistor (MOSFET)-based devices, HfO_2 has already occupied the space of SiO_2 [17]. In 1967, a polysilicon-based floating gate flash memory was invented by D. Kahng and S. M. Sze [18]. Further, to improve the storage capacity and retention characteristics of the future generation of floating gate flash memory devices, integration of metal or semiconductor nanoparticles (NPs) inside the high-k dielectric gate oxide layer has been proposed as a floating gate [19–22]. The devices with embedded metal NPs have the advantages of extensive range of work functions, advanced efficiency, and low operating voltages as compared to the devices with semiconductor NPs [23]. When an array of embedded metal NPs is used as a floating gate, then each isolated particle will store the charge. This gate will hold an overall charge even if few particles lose their charge through some unwanted leakage paths. Hence, such a device will have better retention properties as compared to that of the devices which use continuous metal layer as a floating gate [24]. For large storage capacity and to enhance the retention characteristics, application of metal NPs with large work functions like Silver (Ag), Gold (Au), and Platinum (Pt) has been proposed [25–27]. Among these metal NPs, Au NPs attracted the attention because it is easy to synthesize, and it has greater density of states and large work function (5.1 eV), which generates deep potential well that avoids retention loss of the devices and enhances carrier confinement [28, 29].

Another important application of metal NPs is in the fabrication of Surface Enhanced Raman Spectroscopy (SERS) substrates to enhance the Raman scattering [30]. Metal NPs such as Au and Ag, which can favor plasmonic resonance, have significance in SERS studies for molecular detection [31–34]. The SERS studies mainly deal with the enhancement in electromagnetic field due to the confined surface plasmon resonance. This enhancement in the electromagnetic field is directly related to the size, shape, uniformity, and homogeneity of metal NPs [35, 36]. In recent years, significant enhancement in Raman scattering due to nanosilver-embedded silicon nanowires, Ag and Au NPs with diverse geometries have been reported [37–39].

For creating Au NPs, different deposition techniques such as radio frequency or direct current (RF/DC) sputtering, electron beam (e-beam) evaporation, chemical vapor deposition (CVD), and atomic layer deposition (ALD) have been reported [40–43]. Post-deposition thermal annealing (TA), rapid thermal annealing (RTA), and ion beam irradiation techniques have been used to get good uniformity and high-density Au and Ag NPs [44–46]. Devices with high density of metal NPs will have large charge storage capacity and those with good uniformity will help in improving the reproducibility of device characteristics [47]. RTA and TA techniques have been extensively used to create Au NPs in-between two HfO_2 layers [48–50]. However, thermal annealing and Ion beam irradiation techniques are known to crystallize the tunneling oxide layer which leads to high leakage currents due to tunneling and deteriorate the memory device characteristics, particularly for modern alternate high-k dielectrics like HfO_2

[46, 51–56]. Now, the main challenge is to create high-density metal NPs without affecting the phase of the tunneling oxide layer. Non-thermal processes such as laser annealing (LA) may offer alternate methods to anneal the layers of interest without damaging the substrates and/or the surrounding medium.

In 2016, Nikolaos Kalfagiannis et al. [57] proposed this approach of modifying arrays of NPs by laser-induced self-assembly (MONA-LISA) to produce the pre-determined patterns of metal nanostructures. In 2018, L. Kastanis et al. [58] used LA technique to obtain uniformly spaced Au nanocrystals (Au-NCs) and fabricated n-Si/SiO$_2$/Au-NCs/Y$_2$O$_3$/Au-structured memory devices. LA is a promising technique because it offers a high degree of control over the formation of NPs and has an advantage of minimization of defects in the tunneling oxide layer [59]. Moreover, it can produce uniform Au NPs on/inside the gate oxide layer without damaging it. However, to the best of our knowledge, producing a high-density array of Au NPs on the surface of HfO$_2$ thin films using LA technique and application of these laser-annealed Au NPs in SERS spectroscopy and fabrication of Au NPs-embedded HfO$_2$ gate dielectric-based Metal Oxide Semiconductor (MOS) capacitors, without modifying the phase of HfO$_2$, has not been reported.

In this paper, LA technique is used to synthesize a high-density array of Au NPs on the surface of HfO$_2$ thin films without altering the phase of HfO$_2$. Structural and optical properties of these Au NPs are studied as a function of the number of laser pulses incident on the sample. The leakage current conduction mechanisms have been studied invoking several tunneling mechanisms by examining the leakage current–voltage (I–V) characteristics. Applications of these nanoparticles to SERS and floating gate type memory devices have been investigated.

2 Experimental section

2.1 Synthesis

Thin films of HfO$_2$ ($\sim$ 10 nm) were deposited on boron-doped p-type (1–10 Ωcm) silicon (100) and quartz substrates using e-beam evaporation technique. Before the deposition, substrates were cut into pieces of 1 cm × 1 cm each and cleaned using an ultra-sonication process by dipping in acetone

followed by isopropanol and deionized water for 5 min each. Then, these were dried with nitrogen gas and immediately loaded into the chamber. We used a pellet of HfO$_2$ (99%) as a target material for evaporation. The chamber was evacuated to 1.4×10^{-6}-mbar pressure. 10 standard cubic centimeters per minute (SCCM) of O$_2$ gas were released into the chamber during the deposition of HfO$_2$. In the same chamber, a thin non-continuous layer ($\sim$ 5 nm) of Au was grown on top of these as-deposited HfO$_2$ surfaces using thermal evaporation technique without breaking the vacuum inside the chamber.

2.2 Laser annealing

These samples were subjected to LA using a KrF excimer laser system of wavelength 248 nm (Coherent-Compex Pro 102 F) with 10 Hz repetition rate. Samples were placed normal (90°) to the laser beam during the LA. The laser fluence (300 mJ cm^{-2}) and spot size (1 × 1 cm^2) were maintained same for all the samples. Uniformity, size, shape, and surface density of Au NPs have been controlled by changing the number of laser pulses. Spherical Au NPs have been created on the surface of HfO$_2$ thin films by varying the number of laser pulses from 100 to 500.

2.3 Characterization

Field Emission Scanning Electron Microscopy (FESEM) measurements were performed on as-grown and laser-annealed Au/HfO$_2$ bi-layers deposited on Si to estimate the uniformity and size distribution of Au NPs formed on the surface of HfO$_2$ using Carl ZEISS, FEG, ultra-55. UV–visible absorption measurements (in the range of 300–1000 nm) of Au/HfO$_2$ bi-layers deposited on quartz substrates as a function of number of laser pulses were performed using a UV–visible spectrometer. Grazing incident X-ray diffraction (GIXRD) measurements were performed on the as-grown and laser-annealed Au/HfO$_2$ bi-layers and HfO$_2$ films deposited on Si using Bruker D8 Advance diffractometer with Cu Kα, λ = 1.54 Å. SERS measurements were performed by drop-casting Rhodamine 6G (R6G) dye on top of the as-grown and laser-annealed Au/HfO$_2$ bi-layers deposited on Si. A laser with excitation wavelength of 632 nm and 20 mW power has been used for these measurements using LabRAM HR Evolution –

HORIBA Scientific confocal Raman microscope with 100X magnification.

2.4 Fabrication and characterization of MOS capacitors

Finally, on top of these as-grown and laser-annealed Au NPs produced on the surface of HfO$_2$ thin films, another layer of HfO$_2$ with thickness of around 20 nm was deposited as a blocking layer under the same deposition conditions. Metal contacts of Au were deposited ($\sim$ 100 nm thick and 1 mm in diameter using a shadow mask) as top electrode (TE). Adhesive and conductive Ag paste along with Al foil was used as a bottom electrode (BE). A MOS capacitor without Au NPs inside the oxide layer, i.e., a continuous layer of HfO$_2$ of almost same thickness ($\sim$ 30 nm) is also fabricated under the same deposition conditions. The TE/HfO$_2$ and Si/BE interfaces are expected to behave in the same manner for both the devices with or without Au NPs inside HfO$_2$. Hence, the differences in leakage currents and storage capacity are attributed to the presence or absence of Au NPs. The schematic and final structure of the MOS capacitor is shown in Fig. 1. Electrical characterizations such as leakage current–voltage (I–V) and capacitance–voltage (C–V) were performed using an Agilent technologies (B1500A) semiconductor device analyzer.

3 Results and discussion

3.1 Structural and optical properties of Au NPs

The FESEM images of as-grown and laser-annealed Au/HfO$_2$ bi-layers as a function of number of pulses from 100 to 500 are shown in Fig. 2. These images clearly confirm the formation of Au NPs on their surface. As expected, the as-grown sample shows an incomplete layer of Au with the formation of islands which are randomly oriented. It is well known that an array of Au NPs are produced when such an incomplete Au layer is subjected to heat treatment [44, 49]. Here, the main objective is to attain uniform Au NPs by non-thermal LA technique without affecting the phase of the underneath layer of HfO$_2$. Figure 2 shows that the density of Au NPs increases with increase in the number of laser pulses. Further, the particles attain spherical shape and the average particle size reduces with increasing the number of laser pulses. The statistical study of the size of spherical NPs with increasing number of laser pulses is tabulated in Table 1 and column charts with Gauss fitting are presented in Fig. 3. The mean diameter of spherical NPs in as-deposited Au film is around 21.9 nm, which is decreased to 13.7 nm with increasing the number of laser pulses to 500, whereas the surface density of spherical Au NPs is increased from 3.75×10^{10} to 1.64×10^{11} NPs cm^{-2}. This
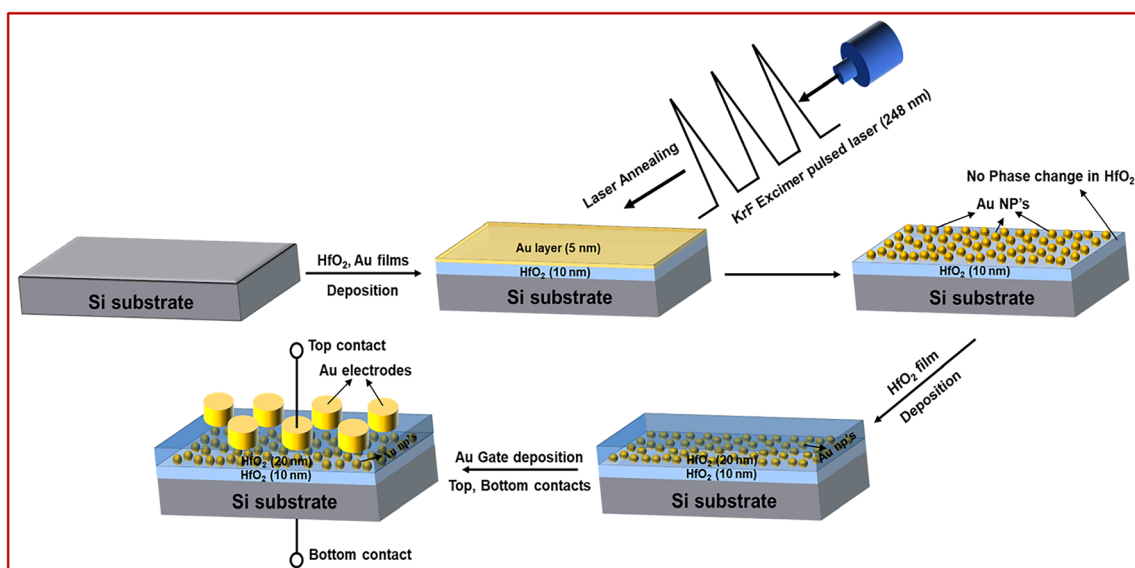

Fig. 1 Schematic representation of creation of high-density spherical Au NPs using LA and fabrication process of Au NPs-embedded HfO$_2$ gate-dielectric-based MOS capacitor

Fig. 2 FESEM images of laser-annealed Au NPs on the surface of HfO$_2$ thin films as a function of number of laser pulses **a** Pristine, **b** 100 pulses, **c** 200 pulses, **d** 300 pulses, **e** 400 pulses, and **f** 500 pulses
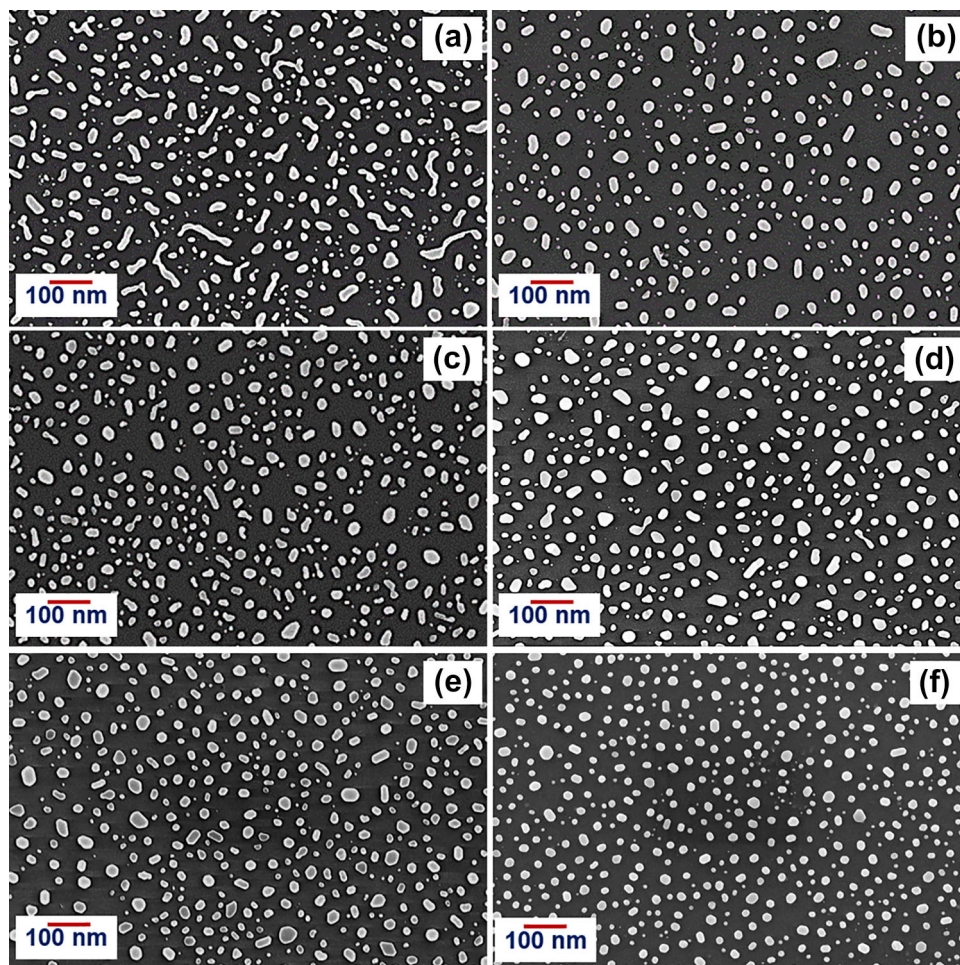

Table 1 Statistical analysis of size and surface density of laser-annealed Au NPs as a function of number of laser pulses

Number of laser pulses	Avg. diameter of Au NPs (nm)	Standard deviation in the size distribution of Au NPs (nm)	Surface density of Au NPs (no. of NPs.cm^{-2})
0	21.9	8.8	3.75×10^{10}
100	23.7	10.1	3.93×10^{10}
200	19.6	7.2	6.12×10^{10}
300	18.5	6.6	9.00×10^{10}
400	17.2	6.3	1.23×10^{11}
500	13.7	4.6	1.64×10^{11}

decrease in the size of spherical Au NPs and standard deviation in size distribution of Au NPs indicates the increase in the uniformity of spherical Au NPs due to LA.

The GIXRD spectra shown in Fig. 4 exhibit the peaks corresponding to the crystalline phases of Au and did not show the introduction of any crystalline phases in HfO$_2$ after laser annealing. This indicates

that the phase of the as-grown and that of the laser-annealed HfO$_2$ films remain same (amorphous in nature) within the experimental limits. The experiment is repeated with pure HfO$_2$ films of thickness ~ 30 nm (without Au layer) which further confirmed that the crystalline phases are not introduced even after the films were subjected up to 2000 laser pulses. While an array of high density of Au

Fig. 3 Size distribution of laser-annealed Au NPs on the surface of HfO$_2$ thin films as a function of number of laser pulses a Pristine, b 100 pulses, c 200 pulses, d 300 pulses, e 400 pulses, and f 500 pulses
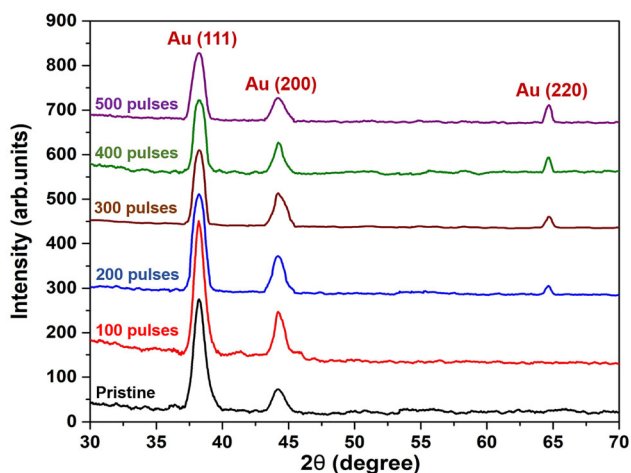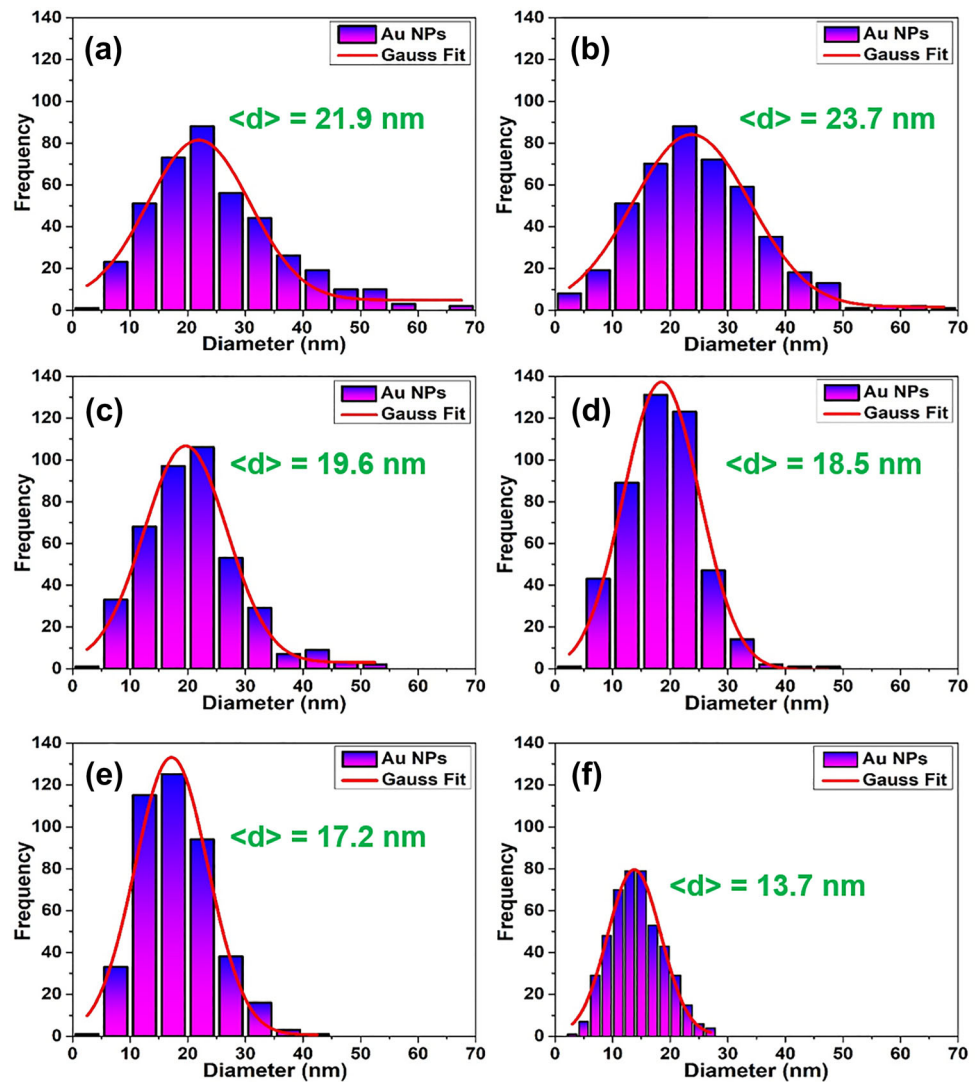

Fig. 4 GIXRD patterns of the as-grown and laser-annealed Au/HfO$_2$ bi-layers as a function of number of laser pulses

NPs was realized even at a lower dose of 500 laser pulses, thus, a high-density array of Au NPs has been synthesized on the surface of HfO$_2$ thin films without significant damage to the underneath film of HfO$_2$. Absorption spectra of pristine and laser-annealed samples are shown in Fig. 5. As the number of laser pulses increases, the absorption peak shifts towards shorter wavelengths with peak narrowing. The Au NPs with smaller size primarily absorb light and show peak near the wavelength of 520 nm, while NPs with larger diameter exhibit increased scattering and show peak shift towards longer wavelengths (red shift) with peak broadening. This further confirms that, as the number of laser pulses increases, the size of Au NPs decreases and uniform spherical Au NPs have been synthesized at 500 laser pulses.
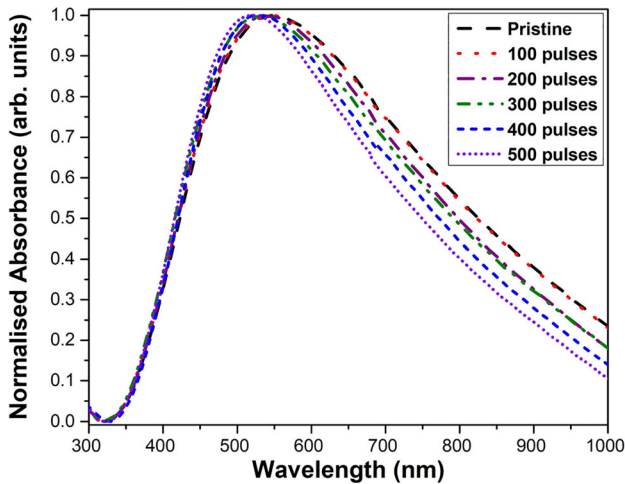
Fig. 5 UV–vis Absorbance spectra of laser-annealed Au NPs as a function of number of laser pulses

SERS measurements were performed on R6G dye (10 nM) in the spectral range from 500 cm^{-1} to 1600 cm^{-1}. For these measurements, a solution of 20 µl R6G of 10 nM concentration is drop casted on top of as-grown and laser-annealed Au NPs and then dried out in the ambient atmosphere. SERS spectra of R6G/HfO$_2$/Si (without Au NPs) and R6G/Au NPs/HfO$_2$/Si (with Au NPs) as a function of number of laser pulses are shown in Fig. 6. Considerable enhancement in Raman signature of R6G dye has been observed for the samples with Au NPs. The intensity of Raman scattering peaks corresponding to
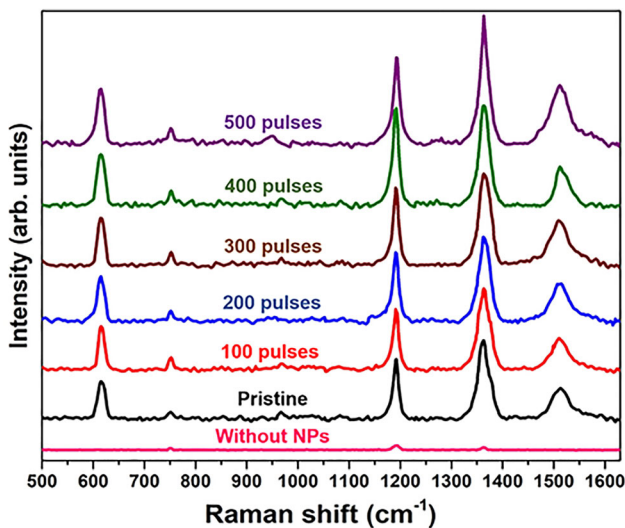
R6G dye is found to be increasing as the number of laser pulses increases. This can be attributed to the observed increase in the surface density of spherical Au NPs, which act as hot spots for SERS, as a function of fluence. For representing the role of Au NPs in SERS substrates, Raman Enhancement Factor (EF) has been calculated using Eq. 1 [60]:

$$EF = \frac{I_{SERS}N_{RS}}{I_{RS}N_{SERS}}, \tag{1}$$

where I$_{SERS}$ and I$_{RS}$ are the intensities corresponding to Raman peaks of R6G molecules adsorbed on Au NPs and on non-SERS samples, respectively. Here, the substrates with Au NPs are considered as SERS, and substrate without Au NPs is considered as non-SERS (R6G/HfO$_2$/Si). N$_{SERS}$ and N$_{RS}$ are the number of R6G molecules on Au NPs and non-SERS substrates which are 10 nM and 10 mM (minimum detectable concentrations of R6G on SERS and non-SERS substrates), respectively. The Raman EF has been estimated for the as-grown and laser-annealed samples as a function of number of laser pulses. The as-grown Au NPs show the EF of 2.6×10^7 corresponding to the Raman peak at ~ 1364 cm^{-1}. The estimated EF and surface density of spherical Au NPs as a function of number of laser pulses is shown in Fig. 7. A systematic increase in the EF has been observed due to increase in the surface density of Au NPs as the number of laser pulses increases. An increased EF of 4.3×10^7 has been observed for the laser-annealed SERS substrate at 500 laser pulses. This not only confirms the formation of an array of high-density spherical Au NPs
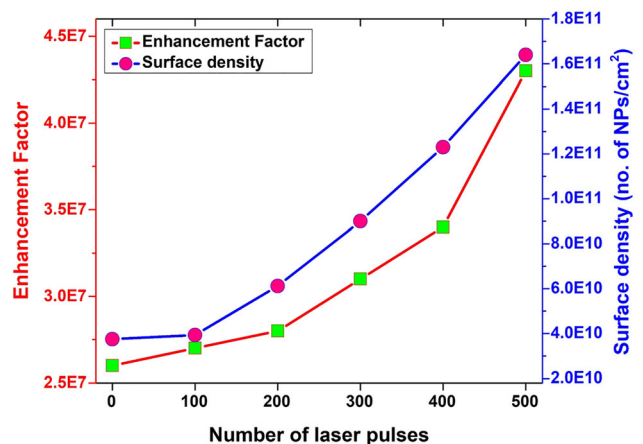

Fig. 6 Raman spectra of R6G on non-SERS substrate (without Au NPs) and SERS substrates (with Au NPs) as a function of number of laser pulses

Fig. 7 Raman EF and surface density of laser-annealed spherical Au NPs as a function of number of laser pulses

but also suggests an alternate non-thermal method to fabricate SERS substrates which offers significant enhancement in the Raman scattering. Hence, LA technique can be used in the fabrication of SERS substrates for molecular detection. Hereafter, the sample which is subjected to LA at 500 laser pulses is used for further application in fabrication of Au NPs-embedded HfO$_2$ gate dielectric-based MOS capacitors.

3.2 Electrical characteristics of MOS capacitors

MOS capacitor has been fabricated using the sample annealed at 500 laser pulses to study electrical characteristics (referred to as "with Au NPs") as shown in Fig. 1. To compare the role of embedded Au NPs in device performance, a MOS capacitor without Au NPs in the HfO$_2$ layer of same thickness ($\sim$ 30 nm) is also fabricated (referred to as "without Au NPs") under the same deposition conditions. The leakage current conduction through gate oxide with and without embedded Au NPs of these MOS capacitors were studied by I–V characteristics as shown in Fig. 8a. As expected, an increase in the leakage current density has been observed for MOS structures with Au NPs when compared to the MOS structures without Au NPs. The charge carriers that tunnel through the gate oxide are responsible for this leakage current and can be elucidated by examining several conduction mechanisms such as direct tunneling (DT), Poole–Frenkel (PF) tunneling, and Fowler–Nordheim (FN) tunneling [61–63]. However, the effects related to spin–orbit coupling are not incorporated in this study as both the electrodes are non-magnetic [11].

The DT mechanism dominates when the charge carriers directly tunnel through the ultra-thin gate oxide layer. However, the thinner oxide layer may deteriorate the data retention capability. The charge retention characteristics can be enhanced and the tunneling probability can be reduced by increasing of barrier height [64]. In the DT mechanism, the limited thickness of modern alternate high-k dielectric thin-film is around 6 nm [65]. Hence, DT is not expected to be significant in this case as the HfO$_2$ film thickness is around 30 nm. Measured I-V characteristics are fitted with theoretical PF and FN tunneling mechanisms using following Eqs. 2 and 3, respectively, to evaluate the contribution from various
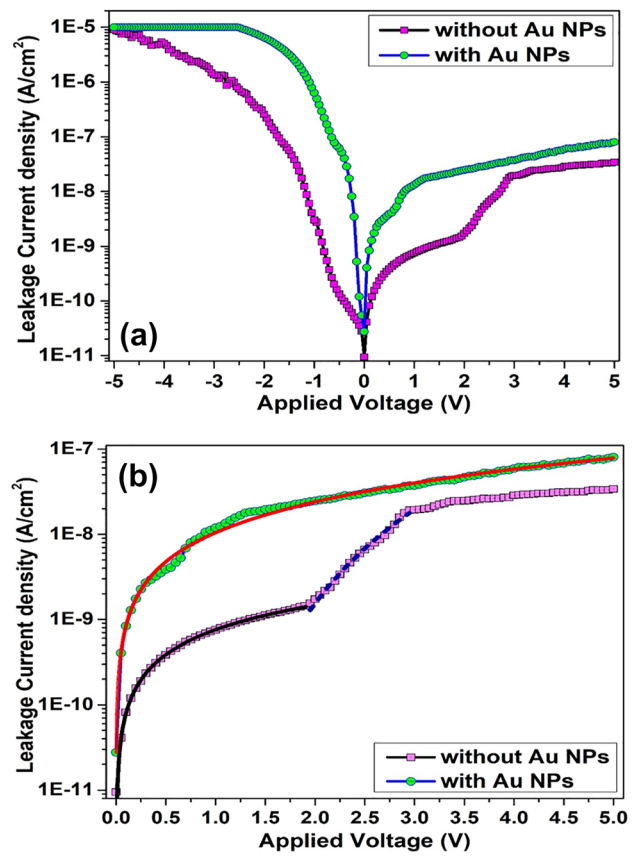

Fig. 8 **a** I–V characteristics of HfO$_2$-based MOS capacitors with and without Au NPs **b** Leakage current characterized by PF and FN tunneling mechanisms (solid lines indicate PF tunneling and dashed line indicates FN tunneling)

tunneling processes to the I-V characteristics [62, 66] (see Fig. 8b, solid lines indicate PF tunneling and dashed line indicates FN tunneling).

$$J_{PF} = EF_{ox}\exp\left[-\frac{q\Phi - \beta\sqrt{F_{ox}}}{\xi KT}\right], \quad (2)$$

$$J_{FN} = \frac{q^3}{16\pi^2\hbar\Phi_b}F_{ox}^2\exp\left[-\frac{4}{3}\frac{\sqrt{2m_{ox}^*}\Phi_b^{3/2}}{\hbar q}\frac{1}{F_{ox}}\right], \quad (3)$$

where F_{ox} is the electric field through the gate oxide, q is the charge of electron, ξ (constant value in between 1 and 2) is the factor that determined by acceptor compensation, Boltzmann's constant (K), Temperature (T), $\hbar$ is the reduced Planck constant, Φ_b is the barrier height among the conduction bands at semiconductor-gate oxide interface and m_{ox}^* is the effective electron mass in the gate oxide.

For the MOS structure without Au NPs, PF tunneling is prominent from 0 V to 1.9 V. Thereafter, FN tunneling dominates from 2.0 V to 2.95 V, and an

exponential increase in the leakage current density has been observed. The FN tunneling mechanism takes place when an applied voltage is effectively high that the electric field cross through a gate oxide decreases the width of the barrier for the charge carriers. At this high applied voltage, FN tunneling mechanism is significant that the electrons can tunnel through the triangular barrier of gate oxide [67]. For the MOS structure with Au NPs, leakage current due to PF tunneling has been observed from 0 V to 5 V. PF tunneling is generally attributed to the charge trapping centers caused by defects in the gate oxide. In the present case, the improved PF tunneling character in laser-annealed devices may be attributed to the possible charge trapping by the embedded Au NPs within the gate oxide layer HfO_2. These traps can limit the channel current flow by the capture or emission of charge carriers. Here, the electrons tunneling through the gate oxide are trapped in the Au NPs and this phenomenon is governed by PF tunneling mechanism.

High-frequency (1 MHz) C–V measurements were performed to study the memory performance (C–V hysteresis) of these MOS capacitors and the C–V hysteresis for the MOS capacitors with and without Au NPs are shown in Fig. 9. For MOS capacitors with Au NPs, an increase in the accumulation capacitance with broadening in the hysteresis has been observed when compared to that of MOS capacitors without Au NPs. This indicates that the charges are trapped in the Au NPs. When a negative bias is applied, the holes which tunnel from the substrate to Au NPs are
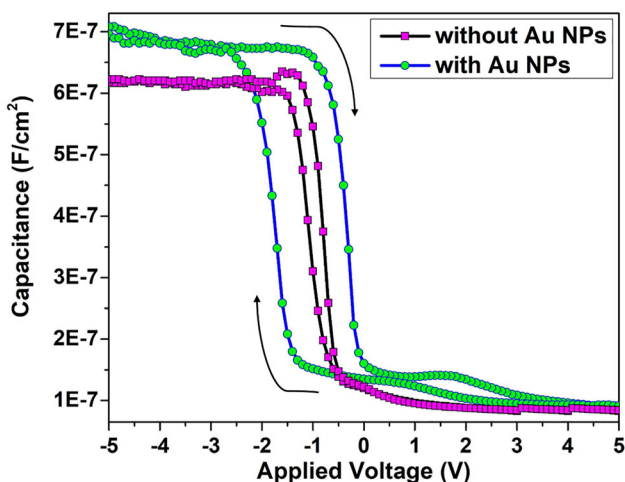
trapped, whereas in accumulation, the electrons tunneling from the substrate are stored in the Au NPs. The C–V curve for the MOS structures without Au NPs shows a narrower hysteresis loop, which indicates that the oxide layer has low density of defects/trapping centers. The hysteresis loop with a large memory window shows the large storage capacity of the device due to embedded Au NPs in the high-k dielectric oxide layer HfO_2. Thus, the high-density array of Au NPs produced on the surface of HfO_2 thin films by using LA can be used in application of microelectronic compatible floating gate type memory devices to enhance the storage capacity.

4 Conclusions

The significant result of this work is the use of LA technique in synthesizing an array of high-density spherical Au NPs on the surface of HfO_2 thin films without affecting the phase of tunneling oxide layer (HfO_2). These spherical Au NPs can be used as charge trapping centers in HfO_2/Au NPs/HfO_2/Si-structured MOS capacitors. Structural characterizations reveal that, as the number of laser pulses increases, the size of spherical Au NPs decreases and a high-density array of Au NPs is realized at 500 laser pulses. UV–visible absorption spectra reveal the peak shifts towards shorter wavelengths with peak narrowing, which indicates an array of high-density uniform spherical Au NPs have been synthesized. These Au NPs show good enhancement ($\sim 10^7$) in Raman signature of standard R6G dye. A systematic increase in the EF has been observed due to the increase in the surface density of Au NPs as the number of laser pulses increases. Hence, these high-density Au NPs can be used as SERS substrates for molecular detection. The leakage current conduction through the gate oxide with and without embedded Au NPs has been studied using PF and FN tunneling mechanisms by examining the I–V characteristics. PF tunneling is prominent for the MOS structures with Au NPs which is attributed to the charge trapping by the embedded Au NPs. The C–V measurements indicate significant broadening in the hysteresis loop which improves the storage capacity of the devices. Thus, the high-density array of Au NPs produced by using LA without affecting the phase of the tunneling oxide layer (HfO_2) can be used in the application of floating gate type memory devices.

Fig. 9 C–V characteristics of HfO_2-based MOS capacitors with and without Au NPs

Acknowledgements

Author contributions

All authors contributed to the study conception and design. Material preparation, data collection, and analysis were performed by KVK, JPG, KRK, KCJR, and SVSNR. The first draft of the manuscript was written by KVK and all authors commented on previous versions of the manuscript. All authors read and approved the final manuscript.

Declarations

Conflict of interest The authors have no relevant financial or non-financial interests to disclose. We hereby declare that the manuscript complies with all ethical values and standards.

Data availability It is available and can be produced anytime.

References

1. J.S. Meena, S.M. Sze, U. Chand, T.-Y. Tseng, Overview of emerging nonvolatile memory technologies. Nanoscale Res Lett. **9**, 526 (2014). https://doi.org/10.1186/1556-276X-9-526

2. S. Wang, C. He, J. Tang, Lu. Xiaobo, C. Shen, Yu. Hua, Du. Luojun, J. Li, R. Yang, D. Shi, G. Zhang, New floating gate memory with excellent retention characteristics. Adv. Electron. Mater. **5**, 1800726 (2019). https://doi.org/10.1002/aelm.201970018

3. J. Li, F. Yan, Solution-processable low-voltage and flexible floating-gate memories based on an n-Type polymer semiconductor and high-k polymer gate dielectrics. ACS Appl. Mater. Interfaces **6**, 12815–12820 (2014). https://doi.org/10.1021/am5028007

4. J. M. Rabaey, Digital integrated circuits: a design perspective, Prentice Hall (1996).

5. G. Wilk, R.M. Wallace, J.M. Anthony, High-k gate dielectrics: current status and materials properties considerations. J. Appl. Phys. **89**, 5243 (2001). https://doi.org/10.1063/1.1361065

6. M.T. Bohr, R.S. Chau, T. Ghani, K. Mistry, The high-k solution. IEEE Spectr. **44**(10), 29–35 (2007). https://doi.org/10.1109/MSPEC.2007.4337663

7. S. Miyazaki, Characterization of high-k gate dielectric/silicon interfaces. Appl. Surf. Sci. **190**, 66–74 (2002). https://doi.org/10.1016/S0169-4332(01)00841-8

8. G.R. Berdiyorov, H. Hamoudi, Effect of insulator thickness on the electronic transport through CNT-HfO_2-Au junction for optical rectenna applications. Surf Interf **22**, 100823 (2021). https://doi.org/10.1016/j.surfin.2020.100823

9. J.H. Choi, Y. Mao, J.P. Chang, Development of Hafnium based high-k materials: a review. Mater. Sci. Eng. R **72**, 97–136 (2011). https://doi.org/10.1016/j.mser.2010.12.001

10. G. Vescio, G. Martin, A. Crespo-Yepes, S. Claramunt, D. Alonso, J. Lopez-Vidrier, S. Estrade, M. Porti, R. Rodriguez, F. Peiro, A. Cornet, A. Cirera, M. Nafria, Low-power, high-performance, non-volatile inkjet-printed HfO_2-based resistive random access memory: from device to nanoscale characterization. ACS Appl. Mater. Interf **11**(26), 23659–23666 (2019). https://doi.org/10.1021/acsami.9b01731

11. C.L. Platt, B. Dieny, A.E. Berkowitz, Spin-dependent tunneling in HfO_2 tunnel junctions. Appl. Phys. Lett. **69**, 2291 (1996). https://doi.org/10.1063/1.117537

12. C.J. Cochrane, P.M. Lenahan, J.P. Campbell, G. Bersuker, A. Neugroschel, Observation of negative bias stressing interface trapping centers in metal gate hafnium oxide field effect transistors using spin dependent recombination. Appl. Phys. Lett. **90**, 123502 (2007). https://doi.org/10.1063/1.2715141

13. S.-L. Jiang, X.-J. Li, Y.-W. Liu, Xi. Chen, Q.-Q. Liu, G. Han, G. Yang, D.-W. Wang, J.-Y. Zhang, J. Teng, Yu. Guang-Hua, Thermally stable anomalous Hall behavior in perpendicular Co/Pt multilayers sandwiched by HfO_2 layers. Appl. Surf. Sci. **360**, 758–761 (2016). https://doi.org/10.1016/j.apsusc.2015.11.060

14. X.L. Zhang, L.F. Liu, W.M. Liu, Quantum anomalous hall effect and tunable topological states in 3d transition metals doped silicene. Sci Rep **3**, 2908 (2013). https://doi.org/10.1038/srep02908

15. Z.F. Jiang, R.D. Li, S.-C. Zhang, W.M. Liu, Semiclassical time evolution of the holes from Luttinger Hamiltonian. Physical Review B **72**, 045201 (2005). https://doi.org/10.1103/PhysRevB.72.045201

16. Y.-H. Chen, H.-S. Tao, D.-X. Yao, W.-M. Liu, Kondo metal and ferrimagnetic insulator on the triangular kagome lattice. Phys. Rev. Lett. **108**, 246402 (2012). https://doi.org/10.1103/PhysRevLett.108.246402

17. R. Chau, S. Datta, M. Doczy, J. Kavalieros, M. Metz, Extended Abstracts of International Workshop on Gate Insulator (IWGI), Japan, Tokyo, 124 (2003). https://doi.org/10.1109/IWGI.2003.159170

18. D. Kahng, S.M. Sze, A floating gate and its application to memory devices. Bell Syst. Tech. J. **46**, 1288–1295 (1967). https://doi.org/10.1002/j.1538-7305.1967.tb01738.x

19. S. Tiwari, F. Rana, H. Hanafi, A. Hartstein, E.F. Crabbe, K. Chan, A silicon nanocrystals based memory. Appl. Phys. Lett. **68**, 1377 (1996). https://doi.org/10.1063/1.116085

20. W. Guan, S. Long, M. Liu, Z. Li, Hu. Yuan, Qi. Liu, Fabrication and charging characteristics of MOS capacitor structure with metal nanocrystals embedded in gate oxide. J. Phys. D: Appl. Phys. **40**, 2754 (2007). https://doi.org/10.1088/0022-3727/40/9/012

21. T. Jiang, Z. Shao, H. Fang, W. Wang, Q. Zhang, D. Wu, X. Zhang, J. Jie, High-performance nanofloating gate memory based on lead halide perovskite nanocrystals. ACS Appl. Mater. Interfaces **11**(27), 24367–24376 (2019). https://doi.org/10.1021/acsami.9b03474

22. M. Olmedo, C. Wang, K. Ryu, H. Zhou, J. Ren, N. Zhan, C. Zhou, J. Liu, Carbon nanotube memory by the self-assembly of silicon nanocrystals as charge storage nodes. ACS Nano **5**(10), 7972–7977 (2011). https://doi.org/10.1021/nn202377f

23. T.T.-J. Wang, C.-L. Chu, I.-J. Hsieh, W.-S. Tseng, Formation of iridium nanocrystals with highly thermal stability for the applications of nonvolatile memory device with excellent trapping ability. Appl. Phys. Lett. **97**, 143507 (2010). https://doi.org/10.1063/1.3498049

24. G. Chakraborty, A. Sengupta, F.G. Requejo, C.K. Sarkar, Study of the relative performance of silicon and germanium nanoparticles embedded gate oxide in metal-oxide-semiconductor memory devices. J. Appl. Phys. **109**, 064504 (2011). https://doi.org/10.1063/1.3555087

25. S. Fakher, M. Alias, P. Sayers, M. Mabrook, High capacity organic memory structures based on PVP as the insulating layer. J. Mater. Sci.: Mater. Electron. **29**, 17644–17650 (2018). https://doi.org/10.1007/s10854-018-9868-4

26. Ch. Sargentis, K. Giannakopoulos, A. Travlos, D. Tsamakis, Fabrication and electrical characterization of a MOS memory device containing self-assembled metallic nanoparticles. Physica E **38**, 85–88 (2007). https://doi.org/10.1016/j.physe.2006.12.024

27. S.A. Ng, K.A. Razak, L.P. Goh, K.Y. Cheong, P.C. Ooi, K.C. Aw, Direct formation of AuNPs thin film using thermal evaporated zinc as sacrificial template in hydrothermal method. J Mater Sci: Mater Electron **25**, 2227–2236 (2014). https://doi.org/10.1007/s10854-014-1863-9

28. S.A. Ng, K.A. Razak, K.Y. Cheong, K.C. Aw, Memory properties of Au nanoparticles prepared by tuning HAuCl₄ concentration using low-temperature hydrothermal reaction. Thin Solid Films **615**, 84–90 (2016). https://doi.org/10.1016/j.tsf.2016.05.003

29. C.W. Tseng, D.C. Huang, Y.T. Tao, Azobenzene-functionalized gold nanoparticles as hybrid double-floating-gate in pentacene thin-film transistors/memories with enhanced response, retention, and memory windows. ACS Appl. Mater. Interfaces **5**, 9528–9536 (2013). https://doi.org/10.1021/am4023253

30. S. Hong, X. Li, Optimal size of gold nanoparticles for surface-enhanced Raman spectroscopy under different conditions. J. Nanomater. **2013**, 790323 (2013). https://doi.org/10.1155/2013/790323

31. G. Dawson, X. Cheng, A. Centeno, Y. Pilyugina, W. Niu, R. Liu, Excellent surface enhanced Raman properties of titanate nanotube-dopamine-Ag triad through efficient substrate design and LSPR matching. J Mater Sci: Mater Electron **32**, 21603–21610 (2021). https://doi.org/10.1007/s10854-021-06669-w

32. M.S.S. Bharati, V.R. Soma, Flexible SERS Substrates for Hazardous Materials Detection: Recent Advances. Optoelectron Adv **4**, 210048 (2021). https://doi.org/10.29026/oea.2021.210048

33. P.G. Bharti, R.K. Soni, R. Raman, Graphene oxide–silver nanocomposite SERS substrate for sensitive detection of nitro explosives. J Mater Sci Mater Electron **31**, 1094–1104 (2020). https://doi.org/10.1007/s10854-019-02621-1

34. S.S.B. Moram, C. Byram, S.N. Shibu, B.M. Chilukamarri, V.R. Soma, Ag/Au nanoparticle-loaded paper-based versatile surface-enhanced Raman spectroscopy substrates for multiple explosives detection. ACS Omega **3**(7), 8190–8201 (2018). https://doi.org/10.1021/acsomega.8b01318

35. V.S. Vendamani, S.V.S.N. Rao, S.V. Rao, D. Kanjilal, A.P. Pathak, Three-dimensional hybrid silicon nanostructures for surface enhanced Raman spectroscopy based molecular detection. J. Appl. Phys. **123**, 014301 (2018). https://doi.org/10.1063/1.5000994

36. S. Calamak, K. Ulubayram, Polyethylenimine-mediated gold nanoparticle arrays with tunable electric field enhancement for plasmonic applications. J. Mater. Sci.: Mater. Electron. **30**, 10013–10023 (2019). https://doi.org/10.1007/s10854-019-01344-7

37. I. Angela, Lopez-Lorente, recent developments on gold nanostructures for surface enhanced Raman spectroscopy: particle shape, substrates and analytical applications. A review. Analytica Chimica Acta **1168**, 338474 (2021). https://doi.org/10.1016/j.aca.2021.338474

38. V.S. Vendamani, S.V.S.N. Rao, A.P. Pathak, S.V. Rao, Robust and cost-effective silver dendritic nanostructures for SERS-based trace detection of RDX and ammonium nitrate. RSC

Adv. **10**(73), 44747–44755 (2020). https://doi.org/10.1039/D0RA08834J

39. V.S. Vendamani, R. Beeram, S.V.S.N. Rao, A.P. Pathak, S.V. Rao, Trace level detection of explosives and pesticides using robust, low-cost, free-standing silver nanoparticles decorated porous silicon. Opt. Express **29**, 30045–30061 (2021). https://doi.org/10.1364/OE.434275

40. S. Horikoshi, N. Matsumoto, Y. Omata, T. Kato, Growth of Au nanoparticle films and the effect of nanoparticle shape on plasmon peak wavelength. J. Appl. Phys. **115**, 193506 (2014). https://doi.org/10.1063/1.4876263

41. M. Mederos, S.N.M. Mestanza, R. Lang, I. Doi, J.A. Diniz, Germanium nanoparticles grown at different deposition times for memory device applications. Thin Solid Films **611**, 39–45 (2016). https://doi.org/10.1016/j.tsf.2016.05.026

42. Ch. Sargentis, K. Giannakopoulos, A. Travlos, D. Tsamakis, Study of charge storage characteristics of memory devices embedded with metallic nanoparticles. Superlattices Microstruct. **44**, 483–488 (2008). https://doi.org/10.1016/j.spmi.2008.03.003

43. Y.K. Mishra, S. Mohapatra, D. Kabiraj, B. Mohanta, N.P. Lalla, J.C. Pivin, D.K. Avasthi, Synthesis and characterization of Ag nanoparticles in silica matrix by atom beam sputtering. Scripta Mater. **56**, 629–632 (2007). https://doi.org/10.1016/j.scriptamat.2006.12.008

44. M. Sriubas, V. Kavaliunas, K. Bockute, P. Palevicius, M. Kaminskas, Z. Rinkevicius, M. Ragulskis, G. Laukaitis, Formation of Au nanostructures on the surfaces of annealed TiO$_2$ thin films. Surfaces and Interfaces **25**, 101239 (2021). https://doi.org/10.1016/j.surfin.2021.101239

45. Y.K. Mishra, D.K. Avasthi, P.K. Kulriya, F. Singh, D. Kabiraj, A. Tripathi, J.C. Pivin, I.S. Bayer, A. Biswas, Controlled growth of gold nanoparticles induced by ion irradiation: an in situ x-ray diffraction study. Appl. Phys. Lett. **90**, 073110 (2007). https://doi.org/10.1063/1.2642824

46. D. Munthala, A. Mangababu, S.V.S.N. Rao, S. Pojprapai, A.P. Pathak, D.K. Avasthi, Swift heavy ion assisted growth of silver nanoparticles embedded in hafnium oxide matrix. J. Appl. Phys. **130**, 044301 (2021). https://doi.org/10.1063/5.0054846

47. R.K. Gupta, D.Y. Kusuma, P.S. Lee, M.P. Srinivasan, Covalent Assembly of Gold Nanoparticles for Nonvolatile Memory Applications. ACS Appl. Mater. Interfaces **3**, 4619–4625 (2011). https://doi.org/10.1021/am201022v

48. V. Mikhelashvili, B. Meyler, S. Yoffis, J. Salzman, M. Garbrecht, T. Cohen-Hyams, W.D. Kaplan, G. Eisenstein, A nonvolatile memory capacitor based on Au nanocrystals with HfO2 tunneling and blocking layers. Appl. Phys. Lett. **95**, 023104 (2009). https://doi.org/10.1063/1.3176411

49. X. Feng, S. Dong, H. Wong, D. Yu, K.L. Pey, K. Shubhakar, W.S. Lau, Effects of thermal annealing on the charge localization characteristics of HfO$_2$/Au/HfO$_2$ stack. Microelectron Reliability **61**, 78–81 (2016). https://doi.org/10.1016/j.microel.2016.02.012

50. A. Mangababu, N. Arun, K.V. Kumar, A.P. Pathak, S.V.S.N. Rao, Metal nanoparticles in dielectric media: physical vapor deposited HfO$_2$ & Ag multilayers for MOS device and SPR applications. AIP Conf Proc **2265**, 030271 (2020). https://doi.org/10.1063/5.0016821

51. A. Srivastava, R.K. Nahar, C.K. Sarkar, Study of the effect of thermal annealing on high-k hafnium oxide thin film structure and electrical properties of MOS and MIM devices. J Mater Sci: Mater Electron **22**, 882–889 (2011). https://doi.org/10.1007/s10854-010-0230-8

52. M. Dhanunjaya, S.A. Khan, A.P. Pathak, D.K. Avasthi, S.V.S.N. Rao, Grain fragmentation and phase transformations in hafnium oxide induced by swift heavy ion irradiation. J. Phys. D: Appl. Phys. **50**, 505301 (2017). https://doi.org/10.1088/1361-6463/aa9723

53. N. Manikanthababu, S. Vajandar, N. Arun, A.P. Pathak, K. Asokan, T. Osipowicz, T. Basu, S.V.S.N. Rao, Electronic excitation induced defect dynamics in HfO$_2$ based MOS devices investigated by in-situ electrical measurements. Appl. Phys. Lett. **112**, 131601 (2018). https://doi.org/10.1063/1.5012269

54. N. Manikanthababu, T. Basu, S. Vajandar, S.V.S.N. Rao, B.K. Panigrahi, T. Osipowicz, A.P. Pathak, Radiation tolerance, charge trapping, and defect dynamics studies of ALD-grown Al/HfO2/Si nMOSCAPs. J Mater Sci Mater Electron **31**, 3312–3322 (2020). https://doi.org/10.1007/s10854-020-02879-w

55. N. Arun, L.D.V. Sangani, K.V. Kumar, A. Mangababu, M.G. Krishna, A.P. Pathak, S.V.S.N. Rao, Effects of swift heavy ion irradiation on the performance of HfO$_2$-based resistive random access memory devices. J Mater Sci: Mater Electron **32**, 2973–2986 (2021). https://doi.org/10.1007/s10854-020-05049-0

56. A. Vinod, M.S. Rathore, S.R. Nelamarri, Role of annealing temperature on charge storage characteristics of Au nanocrystals with HfO$_2$ tunneling and blocking layers. Superlattices Microstruct **120**, 616–628 (2018). https://doi.org/10.1016/j.spmi.2018.04.052

57. N. Kalfagiannis, A. Siozios, D.V. Bellas, D. Toliopoulos, L. Bowen, N. Pliatsikas, W.M. Cranton, C. Kosmidis, D.C. Koutsogeorgis, E. Lidorikis, P. Patsalas, Selective modification of nanoparticle arrays by laser-induced self-assembly (MONA-LISA): putting control into bottom-up plasmonic nanostructuring. Nanoscale **8**, 8236–8244 (2016). https://doi.org/10.1039/C5NR09192F

58. L. Kastanis, J.L. Spear, Ch. Sargentis, N. Konofaos, D. Tsamakis, D.C. Koutsogeorgis, E.K. Evangelou, Memory performance of MOS structure embedded with laser annealed gold NCs. Solid State Electron. **148**, 63–69 (2018). https://doi.org/10.1016/j.sse.2018.07.012

59. A. Siozios, D.C. Koutsogeorgis, E. Lidorikis, G.P. Dimitrakopulos, Th. Kehagias, H. Zoubos, Ph. Komninou, W.M. Cranton, C. Kosmidis, P. Patsalas, Optical encoding by plasmon-based patterning: hard and inorganic materials become photosensitive. Nano Lett. **12**(1), 259–263 (2012). https://doi.org/10.1021/nl2034738

60. E.C. Le Ru, E. Blackie, M. Meyer, P.G. Etchegoin, Surface enhanced Raman scattering enhancement factors: a comprehensive study. J. Phys. Chem. C **111**(37), 13794–13803 (2007). https://doi.org/10.1021/jp0687908

61. K.Y. Cheong, J.H. Moon, H.J. Kim, W. Bahng, Nam-Kyun Kim, Current conduction mechanisms in atomic-layer-deposited HfO_2/nitrided SiO_2 stacked gate on 4H silicon carbide. J. Appl. Phys. **103**, 084113 (2008). https://doi.org/10.1063/1.2908870

62. J.C. Ranuarez, M.J. Deen, C.-H. Chen, A review of gate tunneling current in MOS devices. Microele. Reliab. **46**(12), 1939–1956 (2006). https://doi.org/10.1016/j.microrel.2005.12.006

63. M. Lenzlinger, E.H. Snow, Fowler-Nordheim tunneling into thermally grown SiO_2. J. Appl. Phys. **40**, 278–283 (1969). https://doi.org/10.1063/1.1657043

64. Z. Liu, C. Lee, V. Narayanan, G. Pei, E.C. Kan, Metal nanocrystal memories. I. Device design and fabrication. IEEE Transact Electron Dev **49**, 1606–1613 (2002). https://doi.org/10.1109/TED.2002.802617

65. H. Chen, Ye. Zhou, S.-T. Han, Recent advances in metal nanoparticle-based floating gate memory. Nano Select **2**, 1245–1265 (2021). https://doi.org/10.1002/nano.202000268

66. A. Paskaleva, A.J. Bauer, M. Lemberger, S. Zucher, Different current conduction mechanisms through thin high-k $Hf_xTi_ySi_zO$ films due to the varying Hf to Ti ratio. J. Appl. Phys. **95**, 5583 (2004). https://doi.org/10.1063/1.1702101

67. L. Esaki, Long journey into tunneling. Science **183**, 1149 (1974). https://doi.org/10.1126/science.183.4130.1149